nature physics

Article

https://doi.org/10.1038/s41567-023-02127-y

High-harmonic generation driven by quantum light

Received: 30 May 2022

Accepted: 5 June 2023

Published online: 03 August 2023

Check for updates

Alexey Gorlach[1,5], Matan Even Tzur[2,5], Michael Birk[1,2], Michael Krüger[2], Nicholas Rivera[3,4], Oren Cohen[2] & Ido Kaminer[1]

High-harmonic generation (HHG) is an extreme nonlinear process in which intense pulses of light drive matter to emit high harmonics of the driving frequency, reaching the extreme ultraviolet and X-ray spectral ranges. So far, HHG has always been generated by intense laser pulses that are well described as a classical electromagnetic field. However, the role of the quantum state of light in non-perturbative interactions of intense light with matter has remained unexplored. Here we show that the defining spectral characteristics of HHG, such as the plateau and cutoff, are sensitive to the quantum state of light. While coherent and Fock light states induce the established HHG cutoff law, thermal and squeezed states substantially surpass it, extending the cutoff compared with a coherent light state of the same intensity. Shaping the quantum state of light thus enables the production of far higher harmonics. We develop the theory of extreme nonlinear optics driven by squeezed light, and more generally by arbitrary quantum states of light, introducing the quantum state of the driving field as a degree of freedom.

When an intense laser field interacts with matter in the form of gases[1,2], liquids[3] or solids[4], an extreme nonlinear process known as high-harmonic generation (HHG) may occur. Within this process, high-order harmonics (integer multiples) of the laser frequency are emitted. The HHG process is a tabletop source of extreme UV radiation and attosecond pulses that has found a broad range of applications, including high-resolution imaging[5] and ultrafast spectroscopy[6–13], ultimately giving birth to the field of attosecond science[14,15].

HHG can be described classically via the three-step model[16], where a point-like electron is driven by a classical field: (1) the driving light frees the electron from the atomic nucleus through tunnel ionization; (2) free acceleration of the electron occurs; and (3) the electron recombines with its parent ion. More accurate models[17] of HHG describe the electron quantum mechanically by the time-dependent Schrödinger equation (TDSE). However, both these models and all other approaches used thus far still consider the driving light as a classical electromagnetic field.

In fact, a classical theory of light was so far sufficient to correctly predict the key observed features of HHG, including the plateau in the spectrum (where the intensities of successive harmonics remain approximately constant) and the cutoff (beyond which the harmonic intensities sharply drop). The classical theory of light is successful because HHG experiments require light with very high intensity, which up to now was generated only by laser-like pulses, for which the quantum theory of light is considered unnecessary. Even a laser pulse of just 1 nJ contains billions of photons, a number so high that quantum properties can typically be regarded as unimportant.

For many years, light states with quantum properties such as squeezing and entanglement were thought to be limited to a small number of photons. The entire field of quantum optics has been perceived as solely relevant to low-intensity light, where the number of photons can be resolved. Squeezed light with billions of photons has been seen as impossible experimentally due to the low efficiency of the generation process. However, recent developments in experimental quantum

[1]Department of Electrical and Computer Engineering and Solid State Institute, Technion–Israel Institute of Technology, Haifa, Israel. [2]Department of Physics and Solid State Institute, Technion–Israel Institute of Technology, Haifa, Israel. [3]Department of Physics, Massachusetts Institute of Technology, Cambridge, MA, USA. [4]Department of Physics, Harvard University, Cambridge, MA, USA. [5]These authors contributed equally: Alexey Gorlach, Matan Even Tzur. e-mail: kaminer@technion.ac.il

optics have changed the picture completely[18–24], demonstrating sources of intense thermal and squeezed light that are already intense enough to excite nonlinear optical processes. For example, a bright squeezed vacuum (BSV) state generated by spontaneous parametric downconversion was employed for second-, third- and fourth-harmonic generation[25], and thermal light generated by superluminescent diodes or optical amplifiers was shown to enhance two-photon fluorescence[21] and second-harmonic generation[18], respectively.

Driving HHG with light states such as BSV is within reach with current technology. HHG was demonstrated using femtosecond pulses with energies as low as 200 nJ in optical fibres[26], and with approximately the same energies in solids[4]. When accounting for the typical pulse durations (tens of femtoseconds[26]), the required intensities for HHG are already accessible with pulses of BSV. For example, BSV picosecond pulses with energies of more than 10 μJ were experimentally demonstrated[20], as well as shorter femtosecond BSV pulses with energies of 350 nJ (ref. 23). These advances suggest that driving HHG with quantum light (that is, not a coherent state) is within reach. However, a theory for such an effect is absent. More generally, the non-perturbative interaction between matter and light with non-classical properties has remained unexplored, both theoretically and experimentally.

There are studies that consider quantizing light in the HHG process[27–40]. However, all these works consider the driving light to be a Glauber coherent state, which is the quantum optical description of a conventional laser field. In other words, the input driving field was still considered to be the same field produced by classical high-intensity pulsed lasers. Specifically, ref. 37 made a notable contribution, presenting a theory for HHG driven by arbitrary states of light and analysing the case of a coherent state, whereas the implications for other quantum states remain to be explored. The assumption of the input driving field as a coherent state so far excluded the possibility of driving HHG by squeezed light, or more generally by an arbitrary quantum state of light.

Here we present the concept of HHG driven by squeezed light and take it a step further, developing the theory of HHG driven by any quantum state of light. Specifically, we find that the HHG spectrum is strongly dependent on the quantum state of the driving light and particularly on its Husimi distribution. We show that squeezing of the driver's photonic state drastically extends the most pronounced feature of the HHG spectrum: its cutoff. For Fock states of light, we show that the well-known cutoff remains unchanged, as in HHG driven by coherent states of light. There, the cutoff frequency scales linearly with the intensity of the driving light, as expected from all current (classical or quantum) theories of HHG[16,17,29,31,36]. However, for thermal light and BSV, the linear cutoff scaling is replaced by a power law $\propto I^{2/3}$ of the light intensity, I; hence the spectrum may reach much higher frequencies than with coherent light of the same average intensity (Fig. 1).

To derive these results, we developed a formalism that treats HHG driven by an arbitrary quantum light state in a non-perturbative manner. As we elaborate below, the cutoff law for an arbitrary state is determined by the interplay between tunnel ionization rates and intensity fluctuations. While the tunnelling rate determines the probability of ionization and consequently the HHG cutoff for a fixed classical field intensity, the quantum fluctuations determine the probability of each given intensity. Note that because squeezed and thermal light exhibit a 'heavy tail' in the photon number distribution, the cutoff of the high-harmonic spectrum is substantially extended compared with a narrower distribution of the same average intensity (such as from a coherent or Fock state). For different light states, we formulated analytical formulae that replace the well-known cutoff formula $3.17U_p + I_p$ (where U_p the ponderomotive energy and I_p is the ionization potential) that describes HHG driven by classical fields (that is, coherent states). For example, for HHG driven by BSV, we found a formula $3.05I_p\left(U_p/\hbar\omega_0\right)^{2/3} + I_p$ (where $\hbar\omega_0$ is the energy of a single driving photon), which is in good agreement with numerical calculations of the spectrum using a full quantum theory that we outline below.

Interaction of an atom with an arbitrary quantum light state

In this section we present an analytical formalism that describes the non-perturbative interaction of an atom with an arbitrary light state. We use the term 'atom' to concisely refer to a general quantum mechanical system, as our approach is also applicable to other systems such as electrons in solids undergoing solid-state HHG. Even though the theory considers a single atom, the results also apply to the case of many equivalent atoms (as explained in ref. 36). We derive analytical expressions for the time-dependent density matrix of a joint light–matter system with arbitrary initial conditions for both the interacting material and the incident light. Before discussing the interaction of the atom with an arbitrary light state, it is instructive to revisit its interaction with classical field (a coherent state), which our formalism builds on.

Consider an electron initially in the state $|\phi_i\rangle$ interacting with a classical electromagnetic field. The electric field is given by $\mathbf{E}_\alpha(t) = \frac{i}{2}\boldsymbol{\varepsilon}_{\mathbf{k}\sigma} f(t)\left(\mathcal{E}_\alpha e^{-i\omega_0 t} - \mathcal{E}_\alpha^* e^{i\omega_0 t}\right)$, where $f(t)$ describes the pulse envelope which depends on time t; ω_0 is the central frequency of the driving light; $\boldsymbol{\varepsilon}_{\mathbf{k}\sigma}$ is the unit vector of the polarization which depends on the wavevector $\mathbf{k}$ and the polarization index σ of the electric field. $\mathcal{E}_\alpha$ is the complex classical electric field amplitude ($\mathcal{E}_\alpha^*$ is the complex conjugate of the amplitude), which we denote by a dimensionless complex parameter α that represents the field strength (later defined as the coherent state parameter). The state of the electron $|\phi_\alpha(t)\rangle$ driven by this field satisfies the TDSE, given in the dipole approximation by:

$$i\hbar\frac{\partial|\phi_\alpha(t)\rangle}{\partial t} = \left(\hat{H}_A + \hat{\mathbf{d}}\cdot\mathbf{E}_\alpha(t)\right)|\phi_\alpha(t)\rangle, \tag{1}$$

with the initial condition $|\phi_\alpha(t=0)\rangle = |\phi_i\rangle$. Here, $\hat{H}_A$ is the Hamiltonian of the field-free atom, $\hat{\mathbf{d}} = e\hat{\mathbf{r}}$ is the dipole moment operator and $\mathbf{E}_\alpha(t)$ is the classical field defined above.

The power spectrum of the dipolar emission of $|\phi_\alpha(t)\rangle$ is proportional to the square of the second derivative of the dipole $\left|\ddot{\mathbf{d}}_\alpha(\omega)\right|^2$, where ω is the emission frequency and $\mathbf{d}_\alpha(\omega)$ is the Fourier transform of the dipole moment expectation value $\mathbf{d}_\alpha(t) = \langle\phi_\alpha(t)|\hat{\mathbf{d}}|\phi_\alpha(t)\rangle$. Both $|\phi_\alpha(t)\rangle$ and $\mathbf{d}_\alpha(\omega)$ were obtained here by numerically solving equation (1) (for example, using a third-order split-step operator method[41,42]). Below we show that the semi-classical $\mathbf{d}_\alpha(\omega)$ found using equation (1), which are numerically accessible[17,41,42], are important assets for the computation of the dipolar emission of an atom driven by the intense arbitrary quantum light state. All the details of the numerical calculations are discussed in more detail in Supplementary Section III.

Now we consider the interaction of the atom with an arbitrary light state; that is, represented by an arbitrary density matrix. The main idea was to decompose the initial driving light state into a sum of coherent (classical) light states and then apply the semi-classical approach described above for each coherent state separately. Finally, we employed the linearity of the Schrödinger equation to formulate the density matrix and emission of the complete system as a sum over semi-classical solutions. We considered all the equations in the interaction picture with respect to free-field Hamiltonian $\hat{H}_F = \sum_{\mathbf{k}\sigma}\hbar\omega_{\mathbf{k}\sigma}a^\dagger_{\mathbf{k}\sigma}a_{\mathbf{k}\sigma}$ where $a^\dagger_{\mathbf{k}\sigma}$ and $a_{\mathbf{k}\sigma}$ are the creation and anihilation operators of the light mode $(\mathbf{k},\sigma)$ (Supplementary Section I).

The initial density matrix of the incident light can be written using the generalized Glauber distribution $P\left(\alpha_{\mathbf{k}_0\sigma_0},\beta^*_{\mathbf{k}_0\sigma_0}\right)$ (refs. 43,44):

$$\rho_F(0) = \int d^2\alpha_{\mathbf{k}_0\sigma_0}d^2\beta_{\mathbf{k}_0\sigma_0}P\left(\alpha_{\mathbf{k}_0\sigma_0},\beta^*_{\mathbf{k}_0\sigma_0}\right)\frac{|\alpha_{\mathbf{k}_0\sigma_0}\rangle\langle\beta_{\mathbf{k}_0\sigma_0}|}{\langle\beta_{\mathbf{k}_0\sigma_0}|\alpha_{\mathbf{k}_0\sigma_0}\rangle}\otimes\prod_{(\mathbf{k}\sigma)\neq(\mathbf{k}_0\sigma_0)}|0_{\mathbf{k}\sigma}\rangle\langle 0_{\mathbf{k}\sigma}|. \tag{2}$$

Here, $|\alpha_{\mathbf{k}_0\sigma_0}\rangle$ and $|\beta_{\mathbf{k}_0\sigma_0}\rangle$ are coherent states with complex parameters $\alpha_{\mathbf{k}_0\sigma_0}$ and $\beta_{\mathbf{k}_0\sigma_0}$ for the driving field mode $(\mathbf{k}_0,\sigma_0)$ and frequency ω_0. We assumed that all the other light modes $(\mathbf{k},\sigma)$ were initially in the vacuum state $|0_{\mathbf{k}\sigma}\rangle$ (this can be directly generalized). We note that here

https://doi.org/10.1038/s41567-023-02127-y

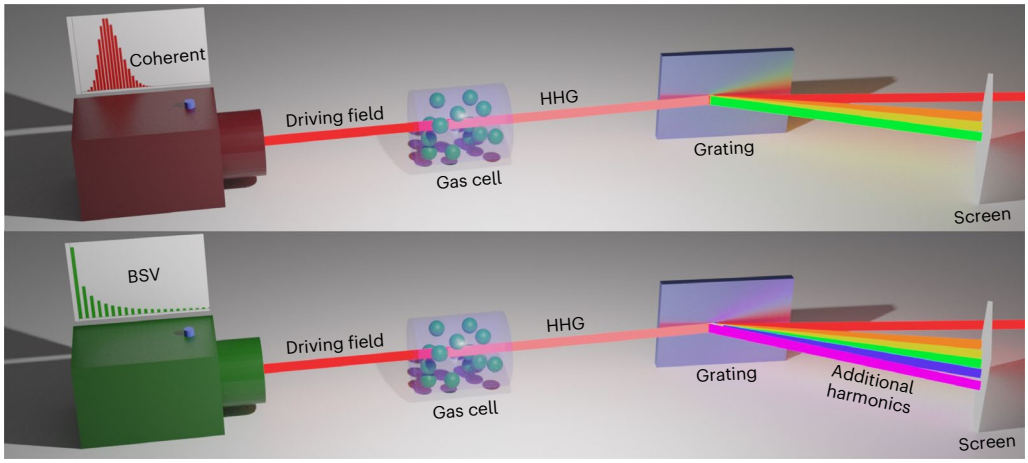

Fig. 1 | An extended spectral cutoff for HHG driven by quantum light states. Schematic illustration of an example emitting system, a gas cell, driven by strong light to produce HHG. The HHG spectrum depends strongly on the quantum state of the driving field. When the system is driven by a BSV state (shown in green), the system emits more harmonics than it would when illuminated by classical coherent light (shown in red), even when that field has the same average intensity, frequency and polarization.

and below, $P\left(\alpha_{\mathbf{k}_0\sigma_0}, \beta^*_{\mathbf{k}_0\sigma_0}\right)$ is time-independent, only describing the initial field state $\rho_F(t=0)$. We employed the generalized Glauber distribution because it is unique for each quantum state, positive and finite for all values of complex α and β (refs. 43,44). This is in contrast with the standard Glauber distribution $P(\alpha)$, which is not a finite and continuous function for some light states (such as squeezed states). The diagonal terms of the Glauber distribution $P(\alpha, \alpha^*)$ are connected with the Husimi distribution $Q(\alpha)$ by $P(\alpha, \alpha^*) = \frac{1}{4\pi} Q(\alpha)$ (ref. 44). We will show below that $Q(\alpha)$ is the key function to determine the outcome of the HHG process.

To obtain the time-dependent density matrix of the joint light–matter system, we needed to solve a more general TDSE with the quantized field $\hat{\mathbf{E}}(t)$:

$$i\hbar \frac{\partial \rho(t)}{\partial t} = \left[\hat{H}_A + \hat{\mathbf{d}} \cdot \hat{\mathbf{E}}(t), \rho(t)\right], \tag{3}$$

where $\rho(t)$ is the joint density matrix of the light–matter system at time t. The initial density matrix is given by $\rho(0) = \rho_F(0) \otimes \rho_A(0)$, where we chose for the examples below $\rho_A(0) = |g\rangle\langle g|$, where $|g\rangle$ is the ground state of the atomic system (this can be directly generalized to any density matrix). $\rho_F(0)$ is defined in equation (2) and can contain any arbitrary driving field state. The quantized electromagnetic field operator in the interaction picture with respect to $\hat{H}_F$ is defined as $\hat{\mathbf{E}}(t) = i\sum_{\mathbf{k},\sigma} \epsilon^{(1)} \boldsymbol{\varepsilon}_{\mathbf{k}\sigma} \left(\hat{a}_{\mathbf{k}\sigma} e^{-i\omega_{\mathbf{k}\sigma} t} - \hat{a}^\dagger_{\mathbf{k}\sigma} e^{i\omega_{\mathbf{k}\sigma} t}\right)$. Here, $\epsilon^{(1)} = \sqrt{\hbar/(2\omega_{\mathbf{k}\sigma} V \varepsilon_0)}$ is the so-called single-photon amplitude that appeared in equation (1), V is the quantization volume, $\boldsymbol{\varepsilon}_{\mathbf{k}\sigma}$ is the unit vector of the polarization, which depends on the polarization index σ and the wavevector $\mathbf{k}$ that satisfies $\omega_{\mathbf{k}\sigma} = c|\mathbf{k}|$.

To solve equation (3) we used the linearity of the Schrödinger equation with respect to the density matrix and solved it separately for each term $\frac{|\alpha_{\mathbf{k}_0\sigma_0}\rangle\langle\beta_{\mathbf{k}_0\sigma_0}|}{\langle\beta_{\mathbf{k}_0\sigma_0}|\alpha_{\mathbf{k}_0\sigma_0}\rangle}$ from the decomposition in equation (2). We combined the separate solutions with weights $P\left(\alpha_{\mathbf{k}_0\sigma_0}, \beta^*_{\mathbf{k}_0\sigma_0}\right)$. More details are presented in Supplementary Section I.

We now connect the classical electric field amplitude $\mathscr{E}_\alpha$ to the coherent state parameter $\mathscr{E}_\alpha = 2\epsilon^{(1)}\alpha$. Interestingly, equation (3) depends on V. However, for typical experimental scenarios, the limit $V\to\infty$ (or $\epsilon^{(1)} \to 0$) should be applied (Supplementary Section I). In the limit $V\to\infty$, the average number of photons $\langle n\rangle$ must also go to infinity for the electric field amplitude $\mathscr{E}_\alpha$ to remain constant. Consequently, in all cases except for extremely small volumes (~1 nm^3 according to Supplementary Section I), $\mathscr{E}_\alpha$ is the only parameter necessary to determine the dynamics.

We derived the joint density matrix of light and the atom in the limit $V\to\infty$ without any additional assumptions. The full mathematical derivation is provided in Supplementary Section I. We considered all modes except the driving field mode $(\mathbf{k}_0, \sigma_0)$, which we traced out in the density matrix and obtained:

$$\rho(t) = \int \mathrm{d}^2\mathscr{E}_\alpha Q(\mathscr{E}_\alpha) |\phi_\alpha(t)\rangle\langle\phi_\alpha(t)| \otimes \prod_{(\mathbf{k}_1\sigma_1),(\mathbf{k}_2\sigma_2)\neq(\mathbf{k}_0\sigma_0)} \left|\gamma^\alpha_{\mathbf{k}_1\sigma_1}\right\rangle\left\langle\gamma^\alpha_{\mathbf{k}_2\sigma_2}\right|, \tag{4}$$

where $Q(\mathscr{E}_\alpha)$ is the Husimi distribution for the complex field amplitude $\mathscr{E}_\alpha$, and $\left|\gamma^\alpha_{\mathbf{k}_1\sigma_1}\right\rangle$ is the coherent state in the mode $(\mathbf{k}_1, \sigma_1)$ with amplitude $\gamma^\alpha_{\mathbf{k}_1\sigma_1} = -\frac{i}{\hbar}\epsilon^{(1)}\mathbf{d}_\alpha(\omega_1)\cdot\boldsymbol{\varepsilon}_{\mathbf{k}_1\sigma_1}$. Equation (4) can be interpreted as the incoherent sum of different coherent solutions with probabilities described by the (always positive) Husimi distribution $Q(\mathscr{E}_\alpha)$. We note that equation (4) defines a density matrix that is always positive, Hermitian and has a well-defined norm. From equation (4) we can easily find the field density matrix $\rho_F(t)$ and the density matrix of the atom $\rho_A(t)$:

$$\rho_F(t) = \mathrm{Tr}_A[\rho(t)] = \int d^2\mathscr{E}_\alpha Q(\mathscr{E}_\alpha) ||\phi_\alpha(t)||^2 \prod_{(\mathbf{k}_1\sigma_1),(\mathbf{k}_2\sigma_2)\neq(\mathbf{k}_0\sigma_0)} \left|\gamma^\alpha_{\mathbf{k}_1\sigma_1}\right\rangle\left\langle\gamma^\alpha_{\mathbf{k}_2\sigma_2}\right|, \tag{5}$$

$$\rho_A(t) = \mathrm{Tr}_F[\rho(t)] = \int d^2\mathscr{E}_\alpha Q(\mathscr{E}_\alpha) |\phi_\alpha(t)\rangle\langle\phi_\alpha(t)|, \tag{6}$$

where $||\phi_\alpha(t)||^2 = \langle\phi_\alpha(t)|\phi_\alpha(t)\rangle$ is the squared norm of the electronic wavefunction $|\phi_\alpha(t)\rangle$.

The time evolution of each $|\phi_\alpha(t)\rangle$ can directly rely on conventional methods for TDSE simulations (equation (1)), developed for HHG driven by classical laser fields. The TDSE for each $|\phi_\alpha(t)\rangle$ also accounts for saturation (ground state depletion). Specifically, the TDSE includes an absorbing boundary condition, causing the wavefunction norm to decay as a function of time. Hence, after several laser cycles (depending on the intensity), the electron is depleted and there is no longer any emission; that is, our formalism accounts for ionization saturation by relying on the conventional methods that were developed in HHG for this purpose. Equation (5) would allow analysis of the full quantum state and all the properties of the emitted light during the HHG process.

https://doi.org/10.1038/s41567-023-02127-y

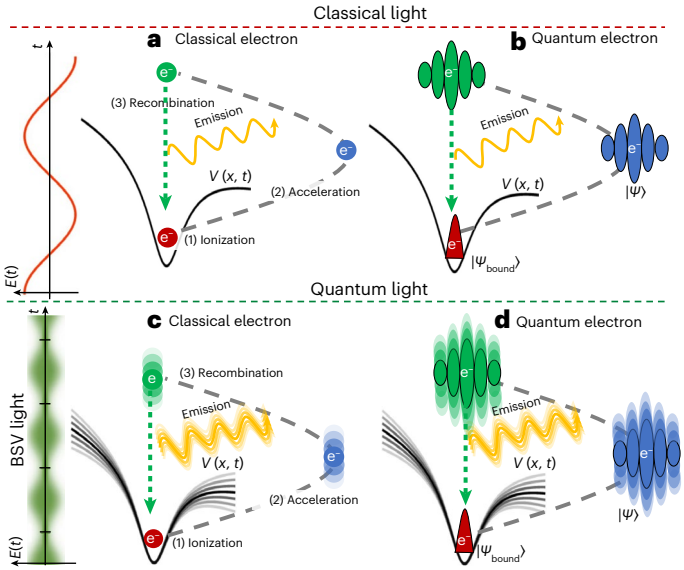

Fig. 2 | Interactions of bound electrons with quantum light. a,**b**, Interactions of a bound electron with classical laser within the three-step model (**a**) or TDSE (**b**). In this case, we can assume that the electric field **E**(*t*) is classical and defined as a function of time. **c**,**d**, In the case of quantum light (for example, BSV), it is impossible to assign the classical **E**(*t*). Instead, we consider a distribution $Q(\mathscr{E}_\alpha)$ of complex fields $\mathscr{E}_\alpha$ and calculate the electron dynamics for each case. The high-harmonic emission results in the statistical average from different electron trajectories, associated with the different electric field amplitudes, as shown in equation (2). In **b** and **d** the electron wavefunction is denoted as $|\Psi\rangle$.

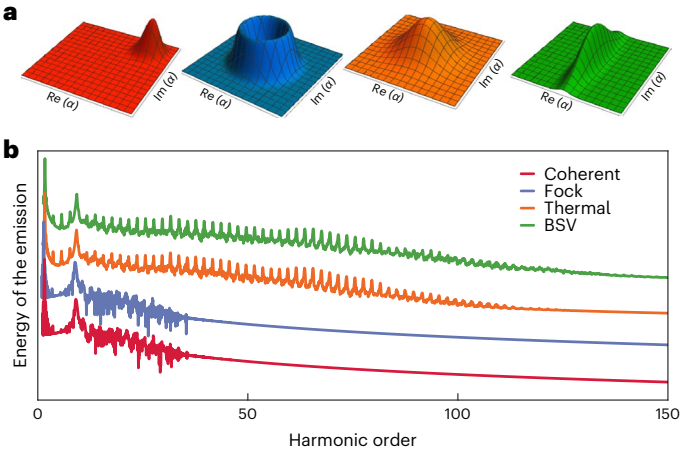

Fig. 3 | Spectra of HHG for different driving light states. a, Husimi distribution $Q(\alpha)$ of the light state, which is sufficient to determine the entire HHG emission spectrum. The Husimi distribution is displayed here for a coherent state (red), Fock state (blue), thermal state (orange) and BSV state (green). **b**, The high-harmonic spectra on a logarithmic scale for the coherent, Fock, thermal and BSV states. The intensities, frequencies and polarizations for all of the driving light states are the same. The spectra are shifted vertically to enhance visibility. Additional spectra for each quantum state are presented in Fig. 4a. In the numerical calculation, the intensity of the driving field is 10^{14} W cm^{-2} and the wavelength of the driving field is $\lambda_0 = 800$ nm.

Importantly, equation (4) shows that the joint density matrix is not separable, although the correlations between the atomic and light subspaces are classical. The absence of entanglement between the atom and light or between different light modes arises from the initial conditions being separable: $\rho(0) = \rho_F(0) \otimes \rho_A(0)$ and from the driving field being a single mode. We expect entanglement in the emission in cases where the initial conditions contain quantum correlations between the emitting atoms[45] or between multiple modes of the driving field.

The $P(\alpha, \beta^*)$ distribution transforms into the $Q(\mathscr{E}_\alpha)$ distribution for $V\to\infty$ and finite field amplitudes (see Supplementary Section I for details). To see why this transformation happens, note that the limit of finite field amplitudes $\mathscr{E}_\alpha \neq \mathscr{E}_\beta$ and large volume $V\to\infty$ implies $|\alpha|, |\beta| \to +\infty$, and then $\langle \mathscr{E}_\alpha | \mathscr{E}_\beta \rangle = \lim_{|\alpha|,|\beta|\to+\infty} \langle \alpha | \beta \rangle = \lim_{|\alpha|,|\beta|\to+\infty} \exp\left(-\frac{1}{2}|\alpha|^2 - \frac{1}{2}|\beta|^2 + \alpha^*\beta\right) = 0$. The orthogonality of states with different field amplitudes $|\mathscr{E}_\alpha\rangle, |\mathscr{E}_\beta\rangle$ is the main reason of why the case of $V\to\infty$ and finite field amplitudes leads to the $Q(\mathscr{E}_\alpha)$ distribution.

Figure 2 illustrates the concept captured by the formalism we developed, focusing on the special case of HHG. This concept is presented by comparing the case of a coherent (classical) drive (top row) and a non-coherent (quantum) drive (bottom row). The $Q(\mathscr{E}_\alpha)$ of the driving field is imprinted on the electron dynamics, and consequently alters the emission spectrum. This $Q(\mathscr{E}_\alpha)$ creates a distribution of electron trajectories, each corresponding to a different field amplitude. The resulting HHG radiation is substantially modified by $Q(\mathscr{E}_\alpha)$. This concept applies regardless of how we treat the electron wavefunction, either classically as a point particle in the three-step model[16] (left column) or semi-classically as a wavefunction in the TDSE[17] (right column). In other words, it does not matter whether we quantize the electron or not, our results show that the quantum light state and particularly $Q(\mathscr{E}_\alpha)$ become imprinted on its dynamics.

Our formalism enables us to treat the electrons as quantum wavefunctions; however, it should also be possible to treat the electrons semi-classically using complex trajectories, while still keeping the driving light quantized (as shown in a recent paper[37] for the case of a coherent state drive). We expect the electron trajectories to be strongly dependent on $Q(\mathscr{E}_\alpha)$. Interestingly, for BSV and thermal light states, the average electric field is $\langle \mathscr{E} \rangle = 0$ and thus the electron trajectories are expected to be completely different from the conventional trajectories of a coherent drive.

The spectrum of HHG from quantum driving

The general equation (5) allows the spectrum $d\varepsilon/d\omega$ to be calculated. To this end, we just calculated $\varepsilon = \sum_{\mathbf{k},\sigma} \mathrm{Tr}\left(\rho_F(t)\, a^\dagger_{\mathbf{k}\sigma} a_{\mathbf{k}\sigma}\right)$, substituting equation (5) for $\rho_F(t)$ (Supplementary Section I):

$$\frac{d\varepsilon}{d\omega} = \frac{\omega^4}{6\pi^2 c^3 \varepsilon_0} \int d^2\mathcal{E}_\alpha ||\phi_\alpha||^2 Q(\mathcal{E}_\alpha) |\mathbf{d}_\alpha(\omega)|^2, \qquad (7)$$

Equation (7) allows us to numerically calculate the HHG spectrum for an arbitrary light state by spanning semi-classical dipoles moments $\mathbf{d}_\alpha(\omega)$. The results of the numerical calculations (Supplementary Section III) for coherent, Fock, thermal and squeezed vacuum light states are shown in Fig. 3, demonstrating striking differences between the different light states. The spectra for parameters that are experimentally accessible at present are discussed in Supplementary Section IV.

According to equation (7), the shape of the spectrum is dependent on the Husimi distribution $Q(\mathscr{E}_\alpha)$ (Fig. 3a). Interestingly, a Fock state does not extend the cutoff despite being strongly non-classical, whereas a thermal state does alter the cutoff. While the coherent and Fock light states lead to approximately the same HHG spectrum, corresponding to their narrow Husimi distributions, thermal and BSV states generate much higher harmonics for the same intensity. This feature shows that for HHG, broad Husimi distributions (for example, thermal and BSV) are preferable over narrow ones (for example, coherent and Fock) for the generation of high frequencies. This preference is surprising, given their vanishing (average) electric field amplitudes, which are usually required to explain the dynamics in the three-step model. We note that the predicted spectral broadening due to thermal and BSV drives is a microscopic effect that arises at the level of each

https://doi.org/10.1038/s41567-023-02127-y

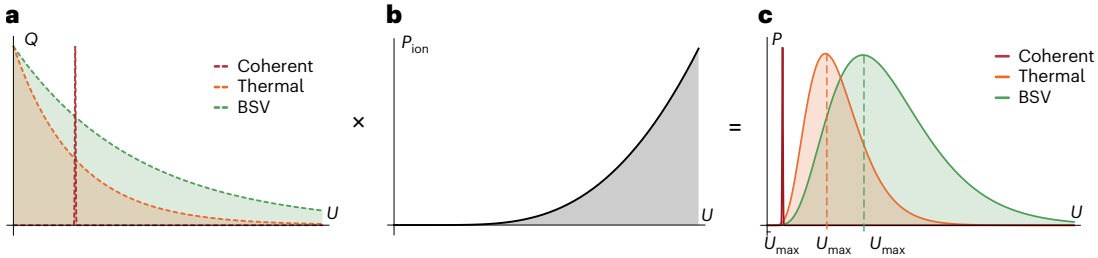

Fig. 4 | The physical origin of the extended cutoffs for thermal and squeezed light states. a, Husimi distribution as a function of the ponderomotive energy U_p, denoted $Q(U)$. **b**, ADK probability of the ionization of an electron in the HHG-emitting system, $P_{ion}(U)$. **c**, Multiplication of $Q(U)$ on $P_{ion}(U)$ gives the effective distribution $P(U)$ of ponderomotive energy that we observe in HHG with an arbitrary light state.

single atom. This prediction can then be combined with the known macroscopic effects in HHG-like phase matching.

It is also interesting to note that the larger the Mandel parameter of the driving field Q_M (ref. 46), the more extended the resulting HHG cutoff is: super-Poissonian thermal light and BSV ($Q_M = \langle n \rangle$ and $Q_M = 2\langle n \rangle + 1$, respectively) have an extended cutoff, whereas Poissonian coherent light ($Q_M = 0$) and sub-Poissonian Fock light ($Q_M = -1$) have the conventional cutoff. Moreover, the spectra in the cases of thermal and BSV drives have more pronounced peaks, more uniform in height (Fig. 3), than the spectra in the cases of coherent and Fock drives. The reason is the averaging of different HHG spectra (equation (7)) over a wide range of $\mathscr{E}_\alpha$ with smooth weights $Q(\mathscr{E}_\alpha)$ in the case of thermal and BSV. This averaging eliminates the blurry and seemingly random features in the individual spectra of each coherent state component $\mathscr{E}_\alpha$. Furthermore, the strength of fluctuations $\langle \Delta n^2 \rangle / \langle n \rangle^2 \cdot 100\%$ for thermal light (~100%) and BSV light (~200%) is much larger than classical shot-to-shot fluctuations in experiments with classical (coherent state) light, which is typically on the order of a few per cent. Thus, experiments with thermal and BSV light are expected to yield considerably different spectra to previous HHG experiments done. To put our results into a broader context, it would be interesting to make a comparison with other nonlinear processes driven by thermal light, such as multiphoton transitions in black-body radiation[39].

The cutoff of HHG from quantum driving

Next we derive analytical cutoff formulae for the HHG spectrum driven by different quantum light states. To do this, we focus on the first step of the three-step model (that is, tunnel ionization). Equation (7) shows that HHG driven by an arbitrary quantum light state can generally be viewed as an incoherent sum of semi-classical HHG processes driven with different complex amplitudes, weighted by the Husimi distribution of the driving light. Broad $Q(\mathscr{E}_\alpha)$ distributions that characterize thermal and squeezed vacuum states extend to extremely high electric field amplitudes but with a monotonically decreasing probability (Fig. 4a). On the other hand, the probability of tunnel ionization by a coherent component $|\alpha\rangle$, and subsequently, HHG, monotonically increases with $|\alpha|$ ($|\mathscr{E}_\alpha| = 2\epsilon^{(1)}|\alpha|$) and can be described by the ADK tunnelling rate $P_{ADK}(\mathscr{E}_\alpha)$ (ref. 47) (Fig. 4b). Overall, the weighted probability of a coherent state component $|\alpha\rangle$ with electric field amplitude $\mathscr{E}_\alpha$ initiating tunnel ionization and HHG is given by the product $P_{ADK}(\mathscr{E}_\alpha)\,Q(\mathscr{E}_\alpha)/\text{norm}$, where $\text{norm} = \int P_{ADK}(\mathscr{E}_\alpha)\,Q(\mathscr{E}_\alpha)\,d^2\mathscr{E}_\alpha$ is a normalization factor (Fig. 4c). This probability obtains a maximum for a particular coherent component α_{max} or $\mathscr{E}_{\alpha_{max}} = 2\epsilon^{(1)}|\alpha_{max}|$, and this coherent component approximately determines the cutoff. That is, the cutoff harmonic is given by $\hbar\omega = I_p + 3.17U_p^{max}$, where $U_p^{max} = e^2\mathscr{E}_{\alpha_{max}}^2/4m\omega_0^2$ is the ponderomotive energy associated with this dominant component $|\alpha_{max}\rangle$.

This approach allowed us to find analytic cutoff formulae for the coherent, Fock, thermal and BSV light states (Supplementary Section II). The narrow Husimi distributions of Fock states yield the same cutoff as for the classical (coherent state) light with the same intensity:

$$\text{cutoff of coherent/Fock states} = 3.17U_p + I_p, \tag{8}$$

In the case of thermal and BSV states:

$$\text{cutoff of thermal state} = 1.92I_p\left(U_p/\hbar\omega_0\right)^{2/3} + I_p, \tag{9}$$

$$\text{cutoff of BSV state} = 3.05I_p\left(U_p/\hbar\omega_0\right)^{2/3} + I_p. \tag{10}$$

In equations (8)–(10), the ponderomotive energy equals to $U_p = e^2\langle\mathscr{E}^2\rangle/4m\omega_0^2$, where $\langle\mathscr{E}^2\rangle = \int d^2\mathscr{E}_\alpha Q(\mathscr{E}_\alpha)\mathscr{E}_\alpha^2$. It is important to note that $\langle\mathscr{E}^2\rangle \neq \langle\mathscr{E}\rangle^2$, and indeed, for both thermal and BSV states the average field is zero $\langle\mathscr{E}\rangle = 0$, and yet the ponderomotive energy is non-zero. This fact shows the inherent limitation of the semi-classical approach[17,41,42], where only the amplitude of the field $\langle\mathscr{E}\rangle$ is important. We also note that such a definition of the ponderomotive energy is consistent with the conventional results of HHG because for intense coherent states, $\langle\mathscr{E}^2\rangle \approx \langle\mathscr{E}\rangle^2$.

The equation for the BSV cutoff differs from the thermal cutoff only by the multiplicative coefficient. However, both of them are very different from the semi-classical cutoff equation (8). Notably, for thermal and BSV distributions, the cutoff energy depends on I_p and scales nonlinearly with U_p. However, the cutoffs in equations (9) and (10) have the same frequency dependence as the conventional cutoff: all of them are proportional to ω_0^{-2}. This scaling shown in Supplementary Section II by substituting the definition of U_p in equations (9) and (10). Figure 5 shows relatively good correspondence between the derived cutoff formulae (equations (8)–(10)) and the numerical simulations.

Discussion

In this work we showed that the spectrum of HHG depends on the Husimi distribution of the driving light. We have demonstrated that the interplay between the Husimi distribution $Q(\alpha)$ and the ADK tunnelling rate determines the cutoff law, which we showed numerically and verified by qualitative analytical calculations.

As it is the most accessible experimental observable, we focused on presenting the HHG emission spectrum in this work. However, our theory allowed us to find the entire density matrix of the atom and the emitted light, as shown in equation (4). Thus, the density matrix of each mode $(\mathbf{k}, \sigma)$ is:

$$\rho_{\mathbf{k}\sigma}(t) = \int \mathrm{d}^2\mathscr{E}_\alpha Q(\mathscr{E}_\alpha)\||\phi_\alpha\rangle\|^2 \otimes |\gamma_{\mathbf{k}\sigma}^\alpha\rangle\langle\gamma_{\mathbf{k}\sigma}^\alpha|. \tag{11}$$

When the driving field has quantum features, the emitted light in the mode $(\mathbf{k}, \sigma)$ will also have some quantum features, directly inherited from the Husimi distribution $Q(\mathscr{E}_\alpha)$ in equation (11). However, it is

https://doi.org/10.1038/s41567-023-02127-y

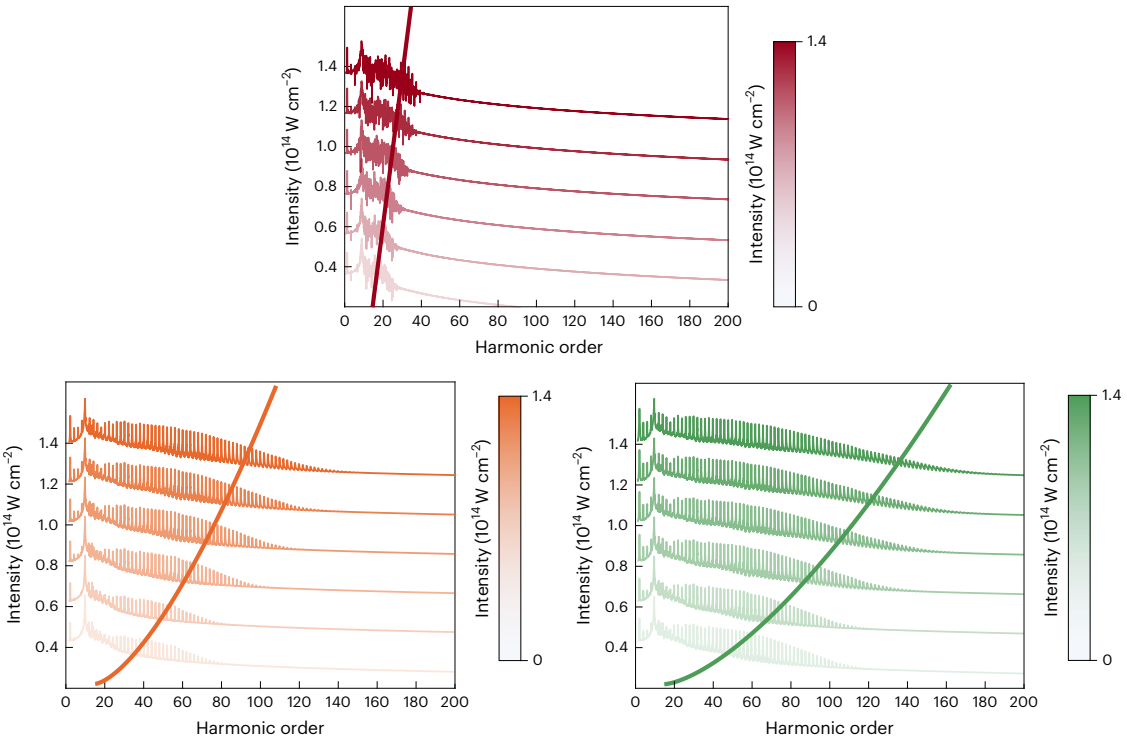

Fig. 5 | Simulations of the high-harmonic spectra for different driving intensities. Numerical simulations of high-harmonic spectra for several different intensities and the analytical cutoff on the same plot for coherent (top), thermal (bottom left) and BSV (bottom right) light states. In the numerical calculation, the wavelength of the driving field is $\lambda_0 = 800$ nm. Thick solid curves in all the plots show the theoretical cutoff predicted by equations (8)–(10).

important to note that the density matrix of the emitted light in equation (11) is different from the density matrix of the driving field $\rho_{\mathbf{k}_0\sigma_0}(t) = \int \mathrm{d}^2\mathscr{E}_\alpha Q(\mathscr{E}_\alpha) \otimes |\mathscr{E}_\alpha\rangle\langle\mathscr{E}_\alpha|$. The reason is that the coherent state components of the emitted light $|\gamma^\alpha_{\mathbf{k}\sigma}\rangle$ (with $\gamma^\alpha_{\mathbf{k}\sigma} \propto \mathbf{d}_\alpha(\omega)\cdot\varepsilon_{\mathbf{k}\sigma}$) strongly differ from the coherent state components of the driving field $|\mathscr{E}_\alpha\rangle$. In fact, $\mathscr{E}_\alpha$ determines $\gamma^\alpha_{\mathbf{k}\sigma}$ via $\mathbf{d}_\alpha(\omega)$, which is highly nonlinear in $\mathscr{E}_\alpha$. The farther this relation is from linear, the more different is the quantum state of the emitted light from to the quantum state of driving field. If the driving field is a coherent state $\rho_{\mathbf{k}_0\sigma_0}(t) = |\mathscr{E}_\alpha\rangle\langle\mathscr{E}_\alpha|$, then the emission is also a coherent state $\rho_{\mathbf{k}\sigma}(t) = |\gamma^\alpha_{\mathbf{k}\sigma}\rangle\langle\gamma^\alpha_{\mathbf{k}\sigma}|$, as expected in conventional HHG and shown in previous works[36,38,40].

The main predictions of our work concern the HHG spectrum, showing that the quantum nature of the drive, as described by the Husimi function, can affect the classical properties of the radiation. Thus, these predictions can be measured by the same techniques used in conventional HHG experiments—for example, using a spectrometer for the high-frequency spectral range. However, we note that the emission spectrum may not be enough to reconstruct the quantum state of the driving field and, instead, higher-order correlations should be measured to enable full reconstruction. From equation (11), we also expect HHG driven by quantum light to also have non-classical properties, such as non-trivial degrees of coherence of the emitted light (Supplementary Section I). Measuring such properties would require quantum optical techniques such as homodyne tomography[48]. It would also be interesting to investigate how the quantum state of the driving field changes the classical electron trajectories, as well as the times of ionization and recombination. We expect substantial dependence of the electron dynamics on the quantum state of the driving field, which could be measured with methods similar to those used in ref. 49.

Our prediction of an extended cutoff for HHG driven by BSV qualitatively agrees with the experimental results for third- and fourth-harmonic generation using BSV[50]. Specifically, ref. 50 demonstrated enhancement in the generation of optical harmonics, showing that the enhancement increases for higher harmonics. Our findings conform with such experiments and generalize them to the non-perturbative regime, predicting an increase in generation efficiency of higher frequencies. Consequently, the control of quantum light states may provide a degree of freedom with which to control the extent of the HHG spectrum. For example, driving with a BSV state generates the same number of harmonics as a coherent state drive with an intensity that is an order magnitude larger (Supplementary Information).

Our predictions are within reach of current experimental capabilities in HHG. In particular, the cutoff behaviour equations (9) and (10) for thermal and BSV light can be observed using classical measurements, such as conventional spectrometry of HHG. In this case, the main obstacle is to generate intense enough pulses of thermal or BSV light. For comparison, classical femtosecond laser pulses with energies as low as 200 nJ and pulse durations of 30 fs were shown to be sufficient for driving HHG in optical fibres[26] and in solids[4]. These pulses correspond to an intensity threshold on the order of 10^{14} W cm^{-2}. Current pulses of BSV generated by spontaneous parametric downconversion[20,23,26] reach approximately 10% of this intensity. Examples include 18 ps BSV pulses with energies of 10 μJ (ref. 20) and shorter femtosecond BSV pulses with energies of 350 nJ (ref. 23). Although stronger BSV pulses are expected to be within reach, we show that even existing BSV pulses should be sufficient for the generation of HHG, because the intensity threshold is lowered by an order of magnitude (Supplementary Information); that is, the quantum statistics extends the cutoff so that lower pulse intensities are sufficient. Intriguingly, even more intense pulses of non-coherent light can be generated by amplification of weaker BSV pulses in solid-state or fibre amplifiers and still maintain the Husimi distribution that extends the HHG cutoff.

Outlook

Looking at the bigger picture, our work sheds light on a fundamental question of how macroscopically quantum light interacts with matter.

It was generally believed that the quantum state of light would not affect the emission spectrum and polarization, only quantum optical observables such as high-order correlations. On the contrary, our work shows that classical characteristics of the HHG process strongly depend on the quantum light state, and particularly on the Husimi distribution $Q(\alpha)$.

We emphasize that the approach described here is applicable far beyond the HHG process. For example, the formalism that we present here can be applied for such effects as above-threshold ionization[51], emission from tips[52,53] and nonlinear Compton scattering[54,55]. It would also be interesting to understand the electron dynamics in all these processes and how it is affected by the quantum state of the driving field. The electron dynamics is fully described by equation (6), where $|\phi_\alpha(t)\rangle$ corresponds to the electron dynamics of the considered process. Specifically, in case of the above-threshold ionization, we expect that the photoelectron spectrum will be extended for thermal and BSV driving field, similar to the HHG spectrum considered here. Together with our results for HHG, these examples hint at a novel research field to explore: extreme nonlinear quantum optics. Extreme nonlinear quantum optics presents exciting opportunities for quantum metrology in X-ray spectroscopy and femtosecond chemistry.

From a fundamental perspective, the quantum optical description of non-perturbative interactions may serve as a guide to harnessing the drive's quantum properties (for example, squeezing and entanglement) to generate attosecond pulses in the XUV spectral range with controllable quantum properties. We envision systems strongly driven by quantum light as new sources of macroscopically entangled light, introducing ideas from quantum information into attosecond science.

Online content

Any methods, additional references, Nature Portfolio reporting summaries, source data, extended data, supplementary information, acknowledgements, peer review information; details of author contributions and competing interests; and statements of data and code availability are available at https://doi.org/10.1038/s41567-023-02127-y.

References

1. McPherson, A. et al. Studies of multiphoton production of vacuum-ultraviolet radiation in the rare gases. *J. Opt. Soc. Am. B* **4**, 595–601 (1987).
2. Ferray, M. et al. Multiple-harmonic conversion of 1064 nm radiation in rare gases. *J. Phys. B* **21**, L31–L35 (1988).
3. Luu, T. T. et al. Extreme-ultraviolet high-harmonic generation in liquids. *Nat. Commun.* **9**, 3723 (2018).
4. Ghimire, S. et al. Observation of high-order harmonic generation in a bulk crystal. *Nat. Phys.* **7**, 138–141 (2011).
5. Kfir, O. et al. Nanoscale magnetic imaging using circularly polarized high-harmonic radiation. *Sci. Adv.* **3**, eaao4641 (2017).
6. Baykusheva, D., Ahsan, M. S., Lin, N. & Wörner, H. J. Bicircular high-harmonic spectroscopy reveals dynamical symmetries of atoms and molecules. *Phys. Rev. Lett.* **116**, 123001 (2016).
7. Frumker, E. et al. Probing polar molecules with high harmonic spectroscopy. *Phys. Rev. Lett.* **109**, 233904 (2012).
8. Neufeld, O. et al. Ultrasensitive chiral spectroscopy by dynamical symmetry breaking in high harmonic generation. *Phys. Rev. X* **9**, 031002 (2019).
9. Ayuso, D. et al. Synthetic chiral light for efficient control of chiral light–matter interaction. *Nat. Photon.* **13**, 866–871 (2019).
10. Heinrich, T. et al. Chiral high-harmonic generation and spectroscopy on solid surfaces using polarization-tailored strong fields. *Nat. Commun.* **12**, 3723 (2021).
11. Neufeld, O. & Cohen, O. Background-free measurement of ring currents by symmetry-breaking high-harmonic spectroscopy. *Phys. Rev. Lett.* **123**, 103202 (2019).
12. Luu, T. T. & Wörner, H. J. Measurement of the Berry curvature of solids using high-harmonic spectroscopy. *Nat. Commun.* **9**, 916 (2018).
13. Silva, R. E. F., Jiménez-Galán, Amorim, B., Smirnova, O. & Ivanov, M. Topological strong-field physics on sub-laser-cycle timescale. *Nat. Photon.* **13**, 849–854 (2019).
14. Paul, P.-M. et al. Observation of a train of attosecond pulses from high harmonic generation. *Science* **292**, 1689–1692 (2001).
15. Krausz, F. & Ivanov, M. Attosecond physics. *Rev. Mod. Phys.* **81**, 163 (2009).
16. Corkum, P. B. Plasma perspective on strong field multiphoton ionization. *Phys. Rev. Lett.* **71**, 1994–1997 (1993).
17. Lewenstein, M., Balcou, P., Ivanov, M. Y., L'Huillier, A. & Corkum, P. B. Theory of high-harmonic generation by low-frequency laser fields. *Phys. Rev. A* **49**, 2117–2132 (1994).
18. Qu, Y. & Singh, S. Photon correlation effects in second harmonic generation. *Opt. Commun.* **90**, 111–114 (1992).
19. Agafonov, I. N., Chekhova, M. V. & Leuchs, G. Two-color bright squeezed vacuum. *Phys. Rev. A* **82**, 11801 (2010).
20. Iskhakov, T. S., Pérez, A. M., Spasibko, K. Y., Chekhova, M. V. & Leuchs, G. Superbunched bright squeezed vacuum state. *Opt. Lett.* **37**, 1919–1921 (2012).
21. Jechow, A., Seefeldt, M., Kurzke, H., Heuer, A. & Menzel, R. Enhanced two-photon excited fluorescence from imaging agents using true thermal light. *Nat. Photon.* **7**, 973–976 (2013).
22. Pérez, A. M. et al. Bright squeezed-vacuum source with 1.1 spatial mode. *Opt. Lett.* **39**, 2403–2406 (2014).
23. Finger, M. A., Iskhakov, T. S., Joly, N. Y., Chekhova, M. V. & Russell, P. S. J. Raman-free, noble-gas-filled photonic-crystal fiber source for ultrafast, very bright twin-beam squeezed vacuum. *Phys. Rev. Lett.* **115**, 143602 (2015).
24. Sharapova, P. R. et al. Properties of bright squeezed vacuum at increasing brightness. *Phys. Rev. Res.* **2**, 13371 (2020).
25. Manceau, M., Spasibko, K. Y., Leuchs, G., Filip, R. & Chekhova, M. V. Indefinite-mean pareto photon distribution from amplified quantum noise. *Phys. Rev. Lett.* **123**, 123606 (2019).
26. Heckl, O. H. et al. High harmonic generation in a gas-filled hollow-core photonic crystal fiber. *Appl. Phys. B* **97**, 369–373 (2009).
27. LaGattuta, K. J. Radiation emitted by a resonantly driven hydrogen atom. *Phys. Rev. A* **48**, 666 (1993).
28. Gauthey, F. I., Garraway, B. M. & Knight, P. L. High harmonic generation and periodic level crossings. *Phys. Rev. A* **56**, 3093 (1997).
29. Gonoskov, I. A., Tsatrafyllis, N., Kominis, I. K. & Tzallas, P. Quantum optical signatures in strong-field laser physics: infrared photon counting in high-order-harmonic generation. *Sci. Rep.* **6**, 32821 (2016).
30. Tsatrafyllis, N., Kominis, I. K., Gonoskov, I. A. & Tzallas, P. High-order harmonics measured by the photon statistics of the infrared driving-field exiting the atomic medium. *Nat. Commun.* **8**, 15170 (2017).
31. Bogatskaya, A., Volkova, E. & Popov, A. Spontaneous transitions in atomic system in the presence of high-intensity laser field. *Europhys. Lett.* **116**, 14003 (2016).
32. Bogatskaya, A. V., Volkova, E. A. & Popov, A. M. Spontaneous emission of atoms in a strong laser field. *J. Exp. Theor. Phys.* **125**, 587–596 (2017).
33. Tsatrafyllis, N. et al. Quantum optical signatures in a strong laser pulse after interaction with semiconductors. *Phys. Rev. Lett.* **122**, 193602 (2019).
34. Gombköto, Á., Varró, S., Mati, P. & Földi, P. High-order harmonic generation as induced by a quantized field: phase-space picture. *Phys. Rev. A* **101**, 13418 (2020).

35. Gombköto, Á., Földi, P. & Varró, S. Quantum-optical description of photon statistics and cross correlations in high-order harmonic generation. *Phys. Rev. A* **104**, 33703 (2021).
36. Gorlach, A., Neufeld, O., Rivera, N., Cohen, O. & Kaminer, I. The quantum-optical nature of high harmonic generation. *Nat. Commun.* **11**, 4598 (2020).
37. Varró, S. Quantum optical aspects of high-harmonic generation. *Photonics*. **8**, 269 (2021).
38. Lewenstein, M. et al. Generation of optical Schrödinger cat states in intense laser–matter interactions. *Nat. Phys.* **17**, 1104–1108 (2021).
39. Varró, S. Coherent and incoherent superposition of transition matrix elements of the squeezing operator. *J. Phys. Conf. Ser.* **2249**, 12013 (2022).
40. Stammer, P. et al. High photon number entangled states and coherent state superposition from the extreme ultraviolet to the far infrared. *Phys. Rev. Lett.* **128**, 123603 (2022).
41. Fleck, J. A., Morris, J. R. & Feit, M. D. Time-dependent propagation of high-energy laser beams through the atmosphere. *Appl. Phys.* **10**, 129–160 (1976).
42. Feit, M. D., Fleck, J. A. Jr. & Steiger, A. Solution of the Schrödinger equation by a spectral method. *J. Comput. Phys.* **47**, 412–433 (1982).
43. Drummond, P. D. & Gardiner, C. W. Generalised P-representations in quantum optics. *J. Phys. A* **13**, 2353 (1980).
44. Kim, M. S., De Oliveira, F. A. M. & Knight, P. L. Properties of squeezed number states and squeezed thermal states. *Phys. Rev. A* **40**, 2494–2503 (1989).
45. Pizzi, A., Gorlach, A., Rivera, N., Nunnenkamp, A. & Kaminer, I. Light emission from strongly driven many-body systems. *Nat. Phys.* https://doi.org/10.1038/s41567-022-01910-7 (2023).
46. Scully, M. O. & Zubairy, M. S. *Quantum Optics* (Cambridge Univ. Press, 1997).
47. Ammosov, M. V. Tunnel ionization of complex atoms and of atomic ions in an altemating electromagnetic field. *Sov. Phys. JETP* **64**, 1191 (1987).
48. Leonhardt, U. & Paul, H. *Measuring the Quantum State of Light*. *Progress in Quantum Electronics* Vol. 19 (Cambridge Univ. Press, 1995).
49. Smirnova, O. et al. High harmonic interferometry of multi-electron dynamics in molecules. *Nature* **460**, 972–977 (2009).
50. Spasibko, K. Y. et al. Multiphoton effects enhanced due to ultrafast photon-number fluctuations. *Phys. Rev. Lett.* **119**, 223603 (2017).
51. Boyd, R. W. *Nonlinear Optics* (Academic, 2020).
52. Krüger, M., Lemell, C., Wachter, G., Burgdörfer, J. & Hommelhoff, P. Attosecond physics phenomena at nanometric tips. *J. Phys. B* **51**, 172001 (2018).
53. Dombi, P. et al. Strong-field nano-optics. *Rev. Mod. Phys.* **92**, 25003 (2020).
54. Bula, C. et al. Observation of nonlinear effects in Compton scattering. *Phys. Rev. Lett.* **76**, 3116 (1996).
55. Mackenroth, F. & Di Piazza, A. Nonlinear Compton scattering in ultrashort laser pulses. *Phys. Rev. A* **83**, 32106 (2011).

Data availability

Source data are provided with this paper. All other data that support the plots within this paper and other findings of this study are available from the corresponding author upon reasonable request.

Code availability

The code is available from the corresponding author upon reasonable request.

Acknowledgements

We acknowledge insightful discussions on related topics with A. Pizzi, R. Ruimy and J. Sloan. The work was supported by the Israel Science Foundation (ISF) under grant no. 830/19, by the Goldman Frontiers in Discovery Grant from the Michigan-Israel Partnership for Research and by the Helen Diller Quantum Center of Technion. The work was also partially supported by European Research Center (ERC) under the European Union's Horizon 2020 research and innovation programme (grant no. 819440 TIMP).

Author contributions

All authors contributed substantially to this work. A.G., M.E.T., I.K. and N.R. developed the initial theoretical ideas. A.G. and M.E.T. performed the numerical calculations. I.K., O.C., M.K., N.R. and M.B. made significant contributions in the development of theoretical concepts and ideas. I.K. and O.C. supervised the project.

Competing interests

The authors declare no competing interests.

Additional information

Supplementary information The online version contains supplementary material available at https://doi.org/10.1038/s41567-023-02127-y.

Correspondence and requests for materials should be addressed to Ido Kaminer.

Peer review information *Nature Physics* thanks the anonymous reviewers for their contribution to the peer review of this work.